V44

X-ray reflectrometry

Fritz Ali Agildere
fritz.agildere@udo.edu

Jan Lucca Viola
janlucca.viola@udo.edu

Experiment: November 4, 2024
Submission: November 15, 2024

TU Dortmund – Department of Physics

Contents

1 Objective

The aim of this experiment is determining the density, thickness and roughness of a thin polysterol film on a silicon wafer. In order to do so, the X-ray reflectivity of the given sample is measured in different configurations and analyzed as described in the following sections.

2 Background

X-rays are a type of ionizing electromagnetic radiation with typical energies in the keV range. Their production inside an X-ray tube relies on the electrostatic acceleration of electrons which then interact with the anode material. The main mechanisms for the emission of energetic photons are the continuous bremsstrahlung resulting from electron deceleration as well as a discrete component emitted after penetration of the inner atomic shells [1, 2].

2.1 Radiation production

The general operating principle of an X-ray tube such as those depicted in Figure 1 relies on electrons emitted from a heating filament, which are then accelerated by a strong electric field to deposit their energy inside the anode material. This process heats up the anode, requiring a sufficient cooling solution and limiting the maximum power output of the construction. Use of rotating anodes effectively spreads the focal spot over a larger area, allowing for better heat dissipation and higher overall beam intensities.

**(a)** Coolidge Tube adapted from [2].   **(b)** Rotating Anode adapted from [2].
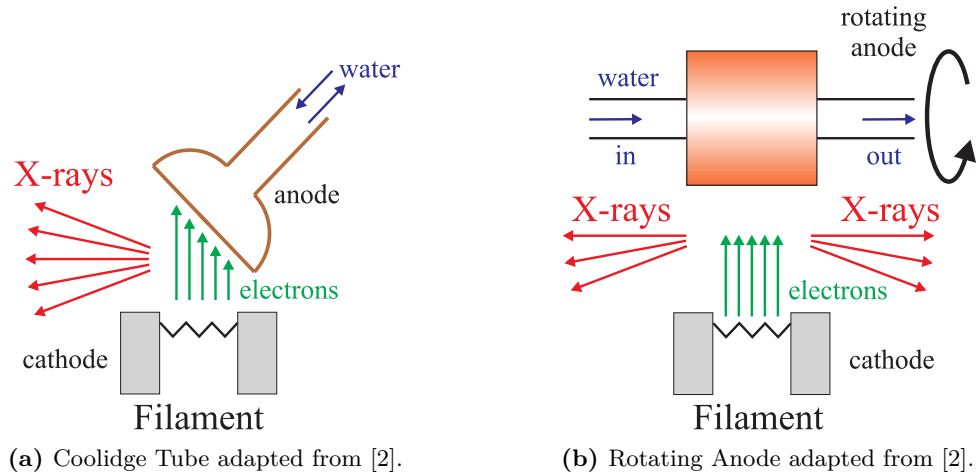
Figure 1: Schematic constructions for different types of X-ray tubes.

The maximum electron kinetic energy available from this process is given by

$$E = eU\,,$$

where e is the elementary charge and U measures the potential drop or voltage set for the experiment. Through scattering processes inside the anode, the inbound charges are decelerated, producing the continuous bremsstrahlung component shown in Figure 2a. Adding to this, incident electrons can transfer large amounts of energy to K shell electrons, freeing them from their tightly bound states to the member atoms and leading to higher energy state electrons from the L and M shells filling the lower state, emitting a photon corresponding to the energy difference as a result. This mechanism is depicted in Figure 2b. As can be seen in Figure 2a, these discrete spikes are much more intense than the superimposed continuous part. To utilize this narrow high intensity component, a Göbel mirror can be used, which parallelizes the X-ray beam while also being designed to extract only the desired spectral window.
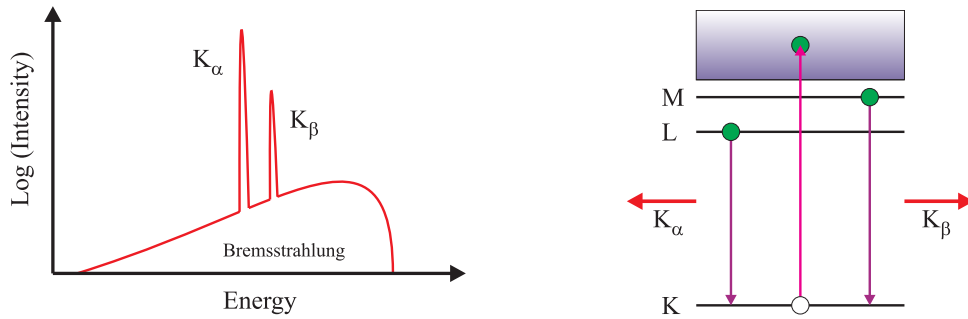
(a) Qualitative emission spectrum adopted from [2].   **(b)** Diagram of energy levels adopted from [2].

Figure 2: Representation of involved physical processes.

2.2 Refractive index

In classical ray optics, the laws of reflection and refraction are

$$\theta_i = \theta_r\,, \qquad\qquad n_1 \cos\theta_i = n_2 \cos\theta_t\,, \tag{1}$$

where n_1 and n_2 are the refractive indices of the two media and $\theta_i, \theta_r, \theta_t$ are the angles of incidence, reflection and transmission as shown in Figure 3.
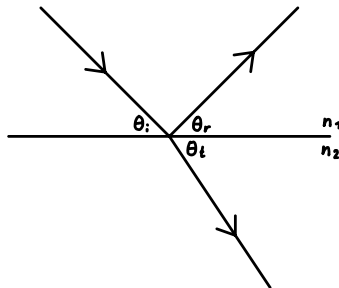
Figure 3: Depiction of reflection and refraction of light rays on a smooth surface.

For X-rays, the refractive index can usually be written as

$$n_2 \equiv n = 1 - \delta \pm i\beta \,,$$

with the extinction coefficient $\beta > 0$ measuring the exponential absorption and a small correction $\delta > 0$ for the dispersion. The choice of $\pm$ depends on the sign convention for the wave vector. From $1 - \delta < 1$ further follows that the phase velocity of X-rays can exceed the speed of light in vacuum c. Because information travels at the group velocity, this does not violate special relativity. Assuming air or vacuum as the surrounding medium, one can set

$$n_1 \equiv 1 \,,$$

resulting in a transition from an optically thick to a thin medium. Accordingly, total reflection occurs for small angles $\theta_i < \theta_c$, with

$$\theta_c = \arccos n$$

defining the critical angle. Proceeding in the small angle approximation, one can expand

$$\cos\theta \cong 1 - \frac{1}{2}\theta^2$$

to second order. Rewriting Snell's law (1) as

$$1 - \frac{1}{2}\theta_i^2 \cong n\left(1 - \frac{1}{2}\theta_t^2\right) = (1 - \delta \pm i\beta)\left(1 - \frac{1}{2}\theta_t^2\right) \cong 1 - \delta \pm i\beta - \frac{1}{2}\theta_t^2$$

yields the relationship

$$\theta_t \cong \sqrt{\theta_i^2 - 2\delta \pm 2i\beta} \,, \tag{2}$$

where products of $\delta, \beta, \theta_t \ll 1$ are ignored in the last step. Similarly, one identifies

$$\theta_c \cong \sqrt{2\delta \mp 2i\beta}$$

by setting $\theta_t = 0$ in (2). Noting $k \to nk$ for the wave propagating in the medium,

$$e^{\pm inkz} = e^{i(1-\delta)kz}e^{-\beta kz}$$

and from this

$$\delta = \frac{2\pi\rho_e r_e}{k^2} \,, \tag{3}$$

$$\beta = \frac{\mu}{2k} \,, \tag{4}$$

relate δ, β to the electron density ρ_e and the absorption coefficient μ via the electron radius $r_e = e^2/m_e c^2$ and $k = 2\pi/\lambda$ [3].

2.3 Fresnel coefficients

By decomposing any electromagnetic wave into linearly polarized components with the electric field oscillations orthogonal (s-polarization) or parallel (p-polarization) to the plane of incidence, one can derive Fresnel's formulae due to continuity of the tangential field component. For the amplitude ratio of reflected to incident ray, this reads as

$$r_s = \frac{\sin\theta_i - n\sin\theta_t}{\sin\theta_i + n\sin\theta_t}$$

for the s-polarized and

$$r_p = \frac{n\sin\theta_i - \sin\theta_t}{n\sin\theta_i + \sin\theta_t}$$

for the p-polarized component [4]. Assuming small angles, an expansion

$$\sin\theta \cong \theta$$

can be made to linear order. With this and by again neglecting products of $\delta, \beta, \theta_i, \theta_t \ll 1$, one finds

$$r_s \cong r_p \cong \frac{\theta_i - \theta_t}{\theta_i + \theta_t} \cong \frac{\theta_i - \sqrt{\theta_i^2 - 2\delta \pm 2i\beta}}{\theta_i + \sqrt{\theta_i^2 - 2\delta \pm 2i\beta}} \equiv r \tag{5}$$

as the amplitude reflectivity, with the corresponding transmittivity $t = 1 - r$. Here, the findings from (2) are used. Accordingly,

$$R = |r|^2 \,, \qquad\qquad T = |t|^2$$

describe the reflectivity and transmittivity in terms of intensity ratios.

2.4 Kiessig fringes

When X-rays encounter a thin layer at low angles, oscillating dips in reflectivity are observed, named Kiessig fringes after their description in [5] as interference minima after multiple reflection. Labeling and conventions from Figure 4 are adopted.
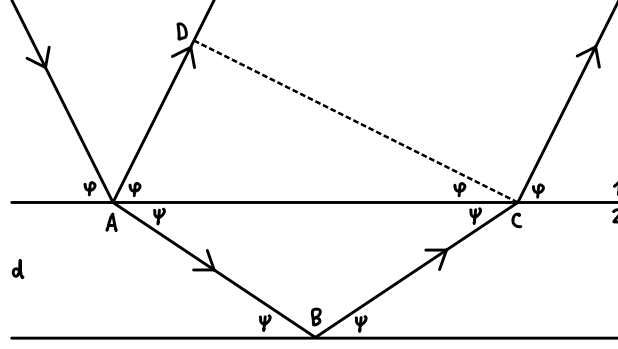
Figure 4: Schematic light paths inside a thin layer atop a substrate producing Kiessig oscillations according to [5].

In the first medium, the waves traverse as distance AD while covering a length $n(AB+BC)$ in the second medium. Their difference is

$$\Delta = n(AB + BC) - AD \,.$$

Expressing AB, BC in terms of d, ψ and applying the small angle approximation,

$$AB = BC = \frac{d}{\sin \psi} \cong \frac{d}{\psi}$$

as well as

$$AC = (AB + BC) \cos \theta$$

for

$$AD = AC \cos \varphi = nAC \cos \psi = \frac{2dn \cos^2 \psi}{\sin \psi} \cong \frac{2dn}{\psi} \cos^2 \psi \cong \frac{2dn}{\psi} - 2dn\psi$$

follow, where the expansion

$$\cos^2 \psi \cong 1 - \psi^2$$

is used. One then obtains

$$\Delta \cong \frac{2dn}{\psi} - \frac{2dn}{\psi} + 2dn\psi \cong 2d\psi \,,$$

where the last step neglects products of $\delta, \beta, \psi \ll 1$. Using (2),

$$\Delta \cong 2d\sqrt{\varphi^2 - 2\delta \pm 2i\beta} \,,$$

which produces an interference minimum for $\Delta = m\lambda$ with $m \in \mathbb{Z}$ and the wavelength λ. When comparing minima,

$$m_{1,2}\lambda \equiv 2d\sqrt{\varphi_{1,2}^2 - 2\delta \pm 2i\beta}$$

5

and by subtracting, rearranging and inserting, one arrives at

$$d = \frac{\lambda}{2}\sqrt{\frac{m_1^2 - m_2^2}{\varphi_1^2 - \varphi_2^2}} , \qquad\qquad \delta = \frac{m_1^2\varphi_2^2 - m_2^2\varphi_1^2}{2(m_1^2 - m_2^2)}$$

for the thickness d and real refractive correction δ. In the case of adjacent minima,

$$d \cong \frac{\lambda}{2(\varphi_1 - \varphi_2)} \tag{6}$$

serves as a reasonable approximation.

2.5 Stratified media

When considering the reflectivity of multiple homogenous layers with sharp boundaries, the transmission and reflection of all lower layers has to be taken into account. To do so, Parratt introduced an exact recursive formalism [4]. This assumes an infinite substrate and surrounding medium, allowing one to start with simple Fresnel reflectivity at the very bottom layer before iterating up towards the surface as sketched in Figure 5.
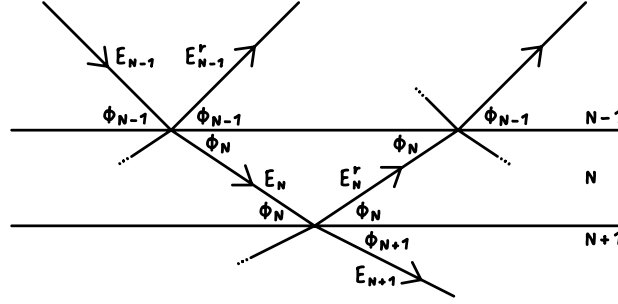
Figure 5: Conceptual visualization of the Parratt algorithm presented in [4].

The wave vector $n_j^2 k^2 = k_j^2 = k_{j,x}^2 + k_{j,z}^2$ in combination with the continuity of the tangential component $k_{j,x} = k_x$ can be used to write

$$k_{j,z}^2 = n_j^2 k^2 - k_{j,x}^2 = n_j^2 k^2 - k_x^2 = (1 - \delta_j \pm i\beta_j)^2 k^2 - k_x^2 \cong (1 - 2\delta_j \pm 2i\beta_j)k^2 - k_x^2 ,$$

where the last step neglects products of $\delta_j, \beta_j \ll 1$, leading to

$$k_{j,z} \cong \sqrt{k_z^2 - 2\delta_j k^2 \pm 2i\beta_j k^2} .$$

Further, one identifies $k_z = k\sin\alpha_i \cong k\alpha_i$ for

$$k_{j,z} \cong k\sqrt{\alpha_i^2 - 2\delta_j \pm 2i\beta_j} , \tag{7}$$

analogous to the result from (2). Adopting the conventions in [6, 7], Fresnel's coefficients can be written as

$$r_{j,j+1} = \frac{k_{j,z} - k_{j+1,z}}{k_{j,z} + k_{j+1,z}} \tag{8}$$

at the boundary between layers j and $j+1$. With this, the Parratt algorithm reads

$$x_j = \frac{r_j}{t_j} = e^{-2ik_{j,z}d_j} \frac{r_{j,j+1} + x_{j+1}e^{2ik_{j+1,z}d_j}}{1 + r_{j,j+1}x_{j+1}e^{2ik_{j+1,z}d_j}} , \tag{9}$$

which for N layers has starting parameters $x_{N+1} = r_{N+1} = 0$ since there are no reflections from the infinte substrate $N+1$ and $t_0 = 1$ as the normalization of the incident ray in the surrounding air or vacuum. The intensity reflectivity is obtained via $R = |r_0|^2 = |x_0|^2$. Accounting for rough boundaries, the specular Fresnel factors are modified such that

$$r_{j,j+1} \to r_{j,j+1}e^{-2k_{j,z}k_{j+1,z}\sigma_{j,j+1}^2}, \tag{10}$$

where deviations following an uncorrelated Gaussian distribution much smaller than the layer thickness d_j are assumed and the roughness is measured by $\sigma_{j,j+1}$.
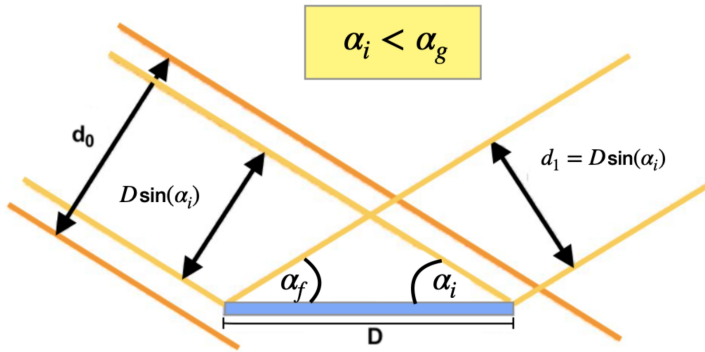
2.6 Geometry factor

At low glancing angles α_i, the beam width $\tilde{d}$ exceeds the effective size $D\sin\alpha_i$ of the sample, meaning the reflected intensity no longer corresponds to the full beam as shown in Figure 6. Correcting for this, the intensity I is divided by the geometry factor

$$G = \begin{cases} \dfrac{D\sin\alpha_i}{\tilde{d}} & \alpha_i < \alpha_g \\ 1 & \alpha_i \geq \alpha_g \end{cases} \tag{11}$$

as $I \to I/G$, with the geometry angle defined by $\tilde{d} = D\sin\alpha_i \cong D\alpha_g$ or

$$\alpha_g \cong \frac{\tilde{d}}{D} . \tag{12}$$

Figure 6: Beam geometry for partial obstruction by the sample at low angles [8].

3 Procedure

As the setup's base the D8 laboratory diffractometer from Bruker-AXS is used. In this diffractometer, which is called $\theta - \theta$ diffractometer, the X-ray tube and detector can be rotated around the probe. The X-ray tube is made of a copper anode and runs on $35\,\mathrm{mA}$ and $35\,\mathrm{kV}$. The first thing to do before starting a measurement is to set up and adjust the used apparatus properly. The following sections provide the needed information to do so and further describe what data are collected.
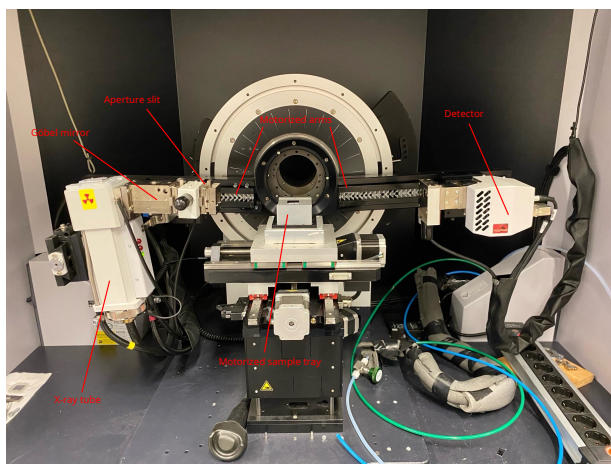
Figure 7: Appartus with labeled components.

3.1 Adjustment of the D8 Diffractometer

The XRD Commander program controls the diffractometer for adjusting the sample and collecting data. The most commonly used interface is the adjust mask. At the top, there is a toolbar with the MoveDrive, Init-Drive, and *Zi* buttons, as well as a button to change the scales of the chart area. On the left side of the adjust mask are the Motor Drives Controls and Generator Controls. At the bottom are the Scan Controls.

To protect the detector from damage, the Absorber must first be set to Auto in the drop-down menu. Do not forget to press the Set button after selecting Auto. After activating the absorber, the geometry of the setup must be adjusted by positioning the X-ray beam, sample, and detector.

The position of the sample can be changed in X, Y, and Z directions using the Motor Drive Controls. Additionally, the position of the detector relative to the tube is changed by driving the 2 motor. The motors are moved by typing the desired position into the Requested value field and setting the checkbox next to it. For example, to move the X-ray tube and the detector to position 0, you first type the value 0 in the corresponding field (2 field) and set the checkmark on the right. In most situations, the program should

set the corresponding checkmark by itself, so it does not have to be set manually. After pressing the Move-Drives button, the motors move to the desired position.

To measure reflectivity, the sample must be brought into the center of rotation of the diffractometer, and the sample surface must be aligned parallel to the X-ray beam. There are three available scan types: the Rocking Curve, the Detector Scan, and the Z-Scan. The measuring method can be selected via the Scantype drop-down menu at the bottom of the adjust mask. Additionally, the scanning ranges and the scan speed must be adjusted for each scan type. After performing the adjustment scans, the data should be saved in raw format, as it will be needed for later analysis.

At the beginning of the adjustment, the sample must be moved out of the beam by changing the Z-coordinate. Furthermore, both the tube and the detector must be moved to an angle of 0°.

3.2 Adjustment of the primary beam

The next thing to do is to adjust the primary beam. For this a detector scan, in which the detector moves in a small angular window around the beam's postion, is needed.

As a result the intensity in dependency of the detector angle should behave like a Gaussian distribution. An example for this behaviour is shown in the top-left plot of Figure 8.

After measuring the distribution, the detectors zero position is set to be at the maximum of intensity. In order to save the new postion the so called *Zi*-Button is clicked. By clicking the *Zi*-Button the systems determines the centre of gravity of the peak and the zero position can then be exactly adjusted.

3.3 Adjustment of the sample position

Similar to the adjustment of the primary beam is the adjustment of the sample postion. By using the X, Y and Z coordinates the probe can be precisely placed in the beams centre. A good adjustment means that the probe is parallel to the beam and shades half of its intensity.

The Z-axis is adjusted first. The height of the probe and the probe's shading can be changed by varying the Z coordinate. If the intensity is at its maximum, the sample is below the beam. The Z value for which the intensity is halved is estimated.

To properly align the sample along the X-axis, an X-scan is initially performed, resulting in a plateau of reduced intensity. This plateau allows flexibility in selecting an examination position on the sample. If adjustments to the sample's X and Z positions yield an intensity of $\frac{1}{2}I_{\max}$, a rocking scan is then conducted to align the Y-coordinate (along the beam direction).

During this scan, the X-ray tube and detector rotate around the sample, maintaining a constant angular sum $i + f = 2$, effectively rotating the sample within the beam. This rotation reveals any tilt of the sample relative to the X-ray beam and is also used to bring the sample's Y-axis to the diffractometer's center of rotation. Ideally, this measurement yields a symmetrical triangular peak in intensity.

In practice, however, the triangle may appear asymmetrical, and the peak intensity may not occur exactly at $\theta = 0$. An asymmetrical triangle suggests that the beam does not strike the sample's center (i.e., the sample is not centered in the rotation axis of the diffractometer). If, for example, the left side of the triangle is flatter than the right, the Y-coordinate should be increased; the reverse adjustment applies otherwise.

In cases where the rocking scan produces a plateau rather than a peak, this indicates misalignment in Z and excessive tilting of the sample. Once the triangle is symmetrical, double-clicking on the maximum intensity value determines its position and sends it to the motors. Using the "Move-Drives" option, the motors adjust to the new positions.

At this point, the X-ray tube and detector are set to the position where the rocking scan identified maximum intensity. This position is typically not exactly at $\theta = 0$. Due to the parallel alignment of the X-ray beam, the sample is no longer perfectly centered within the beam. Thus, a new Z-scan is necessary to re-center the sample to half the beam shading.

Next, a second rocking scan is performed at an angle of $2\theta = 0.3°$ to further refine the sample alignment within the beam. If a clear reflection is visible, the angle of incidence and emergence can be set to $0.15°$ by pressing the *Zi* button and entering 0.15 in the theoretical position field.

Finally, a third Z-scan can refine the half-shading position by locating the maximum of the intensity curve, indicating the complete reflection of the primary beam within a particular height range Z. At this point, an angled Z-scan is conducted Figure 9. The scan range should be close to zero, and the maximum intensity is selected by double-clicking the curve's center of gravity and moving to the corresponding Z-position. For finer adjustments, a final rocking scan is performed at $2\theta = 0.5°$, using the *Zi* key and entering 0.25 in the theoretical position input field to calibrate the angles of incidence and reflection.

Every additional information needed for the measurements is shown in Figure 10.

3.4 Measurement of polymer coated silicon wafer

Now the actual measurement of the silicon wafer can start. The angles of incidence (i) and detection (f) are equal for this scan, which uses the Omega/2Theta scan type. A scan range from 0° to 25° can be selected with a recommended step width of 0.005° and a measuring time of at least 5 seconds per step.
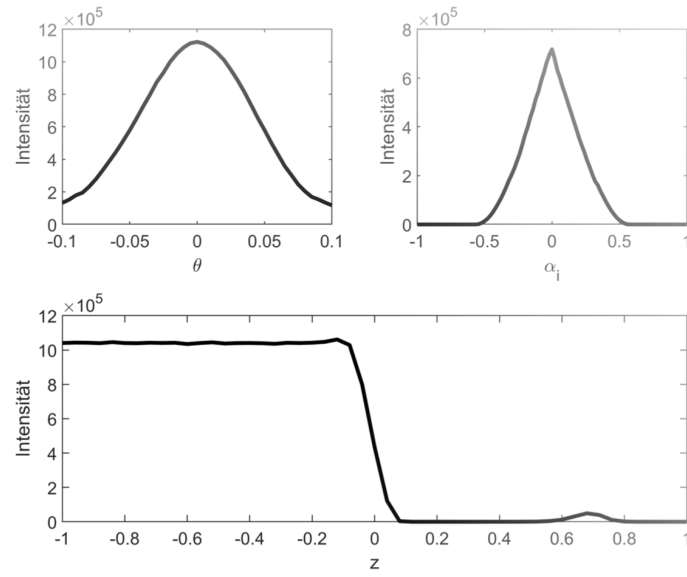
Figure 8: Example measurements of different scantypes needed for the proper adjustment of the apparatus. Top left: Detector scan for beam adjustment, Top right: Rockingscan for *Y*-axis adjustment, Bottom: Z-Scan for sample position [8].
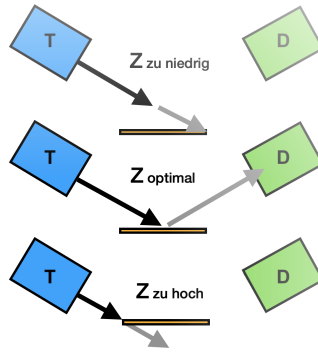
Figure 9: Z-Scan for $2\theta = 0.3°$ [8].

Type	Range	Step size	Measuring time per mesuring point [s]
Detector scan	-0.5 to 0.5	0.02	1
Z-Scan	-1 to 1	0.04	1
X-Scan	-20 to 20	1	1
Rockingscan 2θ = 0	-1 to 1	0.04	1
Z-Scan	-0.5 to 0.5	0.02	1
Rockingscan 2θ = 0.3	0 to 0.3	0.005	1
Z-Scan 2θ = 0.3	-0.5 to 0.5	0.02	1
Rockingscan 2θ = 0.5	0.2 to 0.5	0.005	1

Figure 10: Table with additional information for the adjustment [8].

11

To obtain the true reflectivity, a diffuse scan, which measures scattered radiation, must also be performed. For this scan, the detector angle is offset by 0.2° relative to the incidence angle, using the same step size. All data should be saved in raw format, converted with the program File Exchange, and stored on a USB stick. This completes the measurement process, and the data are ready for analysis.

For smaller angles α_i the beam can be wider than the sample resulting in lower intensities. Its useful to define the angle α_g which is defined as the geometry angle at which the beam hits the whole surface of the wafer. For smaller angles a correction is needed. The intensity for α_i is expanded by $G = \frac{D \sin \alpha_i}{d_0}$ with the beam width $D \sin \alpha_i$ and the total beam width d_0.

4 Results

To analyse the measured data, the Python [9] packages NumPy [10] and SciPy [11] are used, with Matplotlib [12] generating the graphical presentation and Uncertainties [13] allowing for automated linear order propagation of errors obtained from fit functions. The code is included in the appendix.

4.1 Adjustment

A modified Gaussian distribution of the form

$$G(\alpha_i; a, b, \mu, \sigma) = ae^{-(\alpha_i - \mu)^2 / 2\sigma^2} + b$$

is fitted to the primary beam profile, where a and b account for the amplitude and background, respectively. Since the intensity I is given in arbitrary units, it is normalized via $I \rightarrow I/I_{\max}$ for all following measurements.
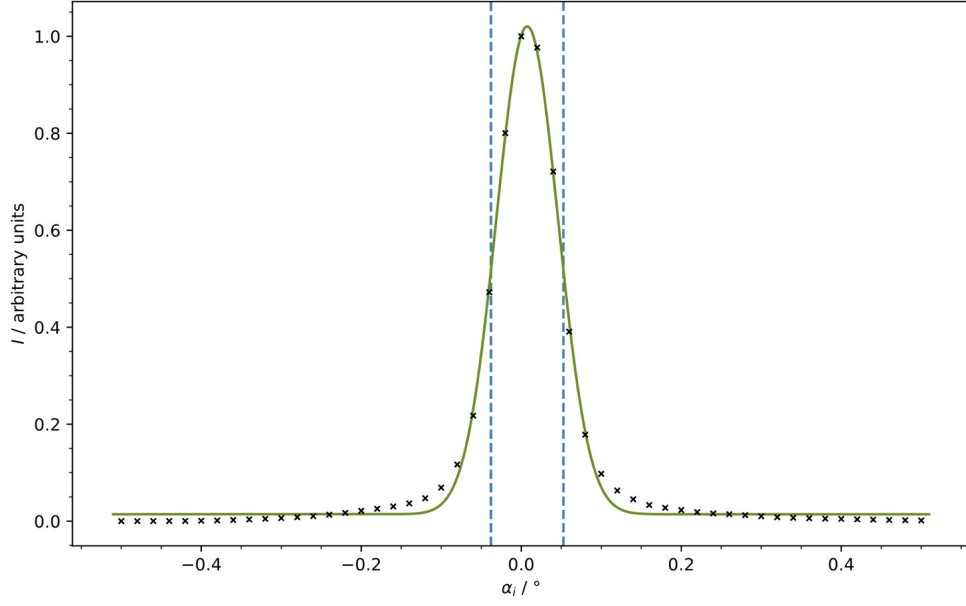
Figure 11: Detector-Scan with fitted Gaussian and marked half maximum positions.

The curve fit to this function shown in Figure 11 yields parameters

$$a = 1.01 \pm 0.01 , \qquad\qquad b = 0.014 \pm 0.002 ,$$
$$\mu = (0.0074 \pm 0.0004)° , \qquad\qquad \sigma = (0.0385 \pm 0.0005)° .$$

One then finds the maximum at $\alpha_{i,\mathrm{max}} = \mu$ as $G(\alpha_{i,\mathrm{max}}) = 1.02 \pm 0.01$ and full width half maximum at $\alpha_{i,\mathrm{fwhm}}^{\pm} = \mu \pm \sigma\sqrt{2\ln 2}$ with

$$\alpha_{i,\mathrm{fwhm}}^{+} = (-0.0528 \pm 0.0007)° , \qquad \alpha_{i,\mathrm{fwhm}}^{-} = (-0.0379 \pm 0.0007)° .$$

Following the detector calibration, the sample position is adjusted. When adjusting the vertical coordinate, one identifies the difference between maximum to minimum intensity, representing zero to full beam obstruction, with the beam width. As indicated in Figure 12, a value

$$\tilde{d} = (0.24 \pm 0.06)\,\mathrm{mm}$$

is determined.
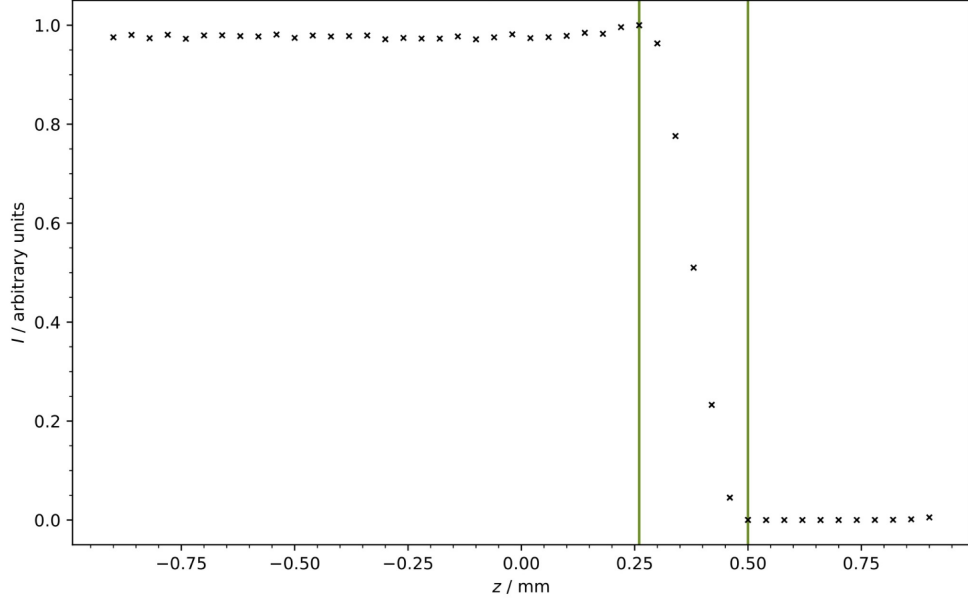
Figure 12: Z-Scan with indicated beam width.

From the intensity valley during horizontal shifting, Figure 13 leads to a sample size

$$D = (21 \pm 3)\,\mathrm{mm}\,,$$

which is in agreement with the literature value $D = 20\,\mathrm{mm}$ [8]. From equation (12) follows a geometry angle
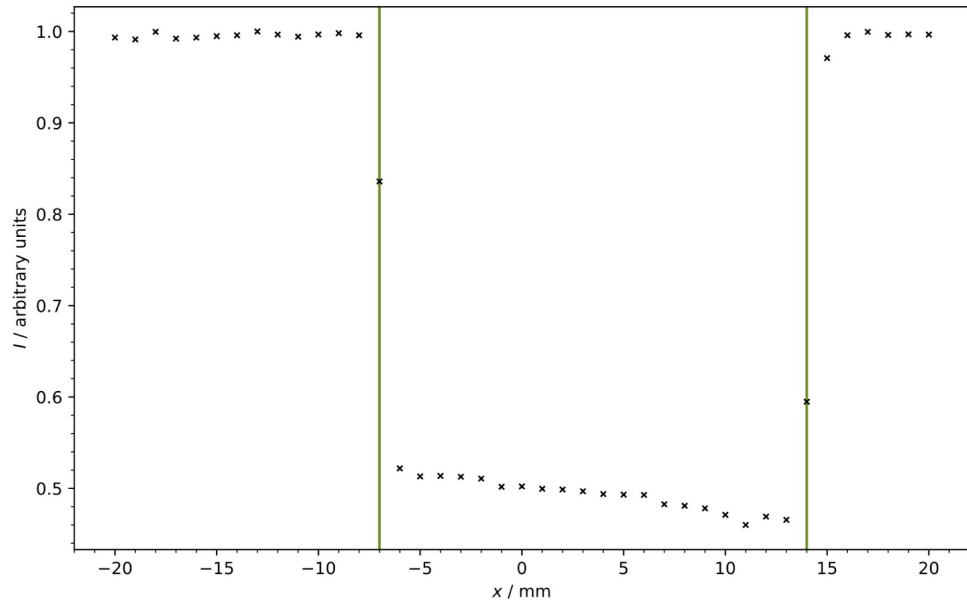
$$\alpha_{g,1} = (0.7 \pm 0.2)^\circ\,.$$

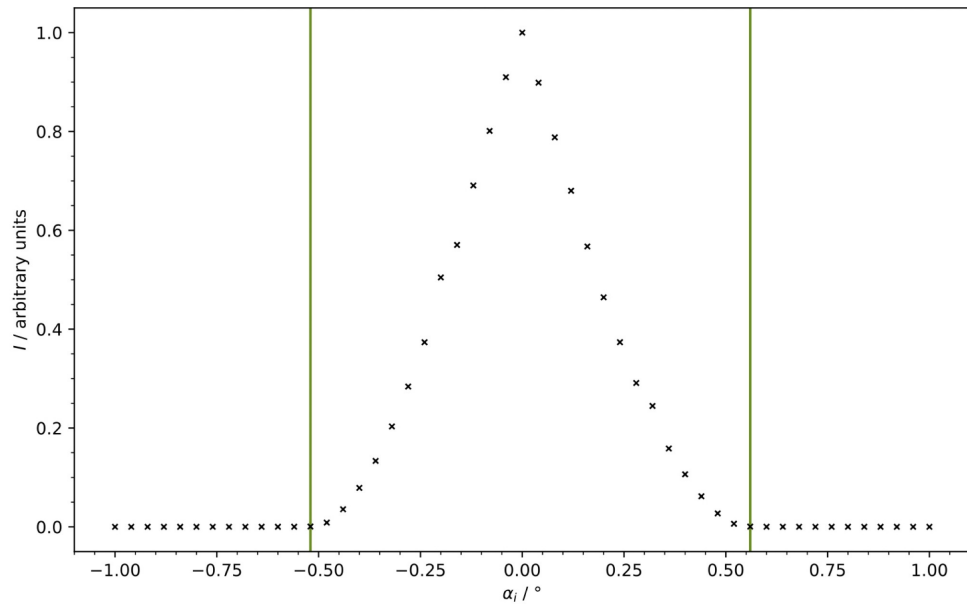Reading the geometry angle from Figure 14, a somewhat lower value of

$$\alpha_{g,2} = (0.54 \pm 0.03)^\circ$$

is obtained, though it still falls inside the uncertainty of the previous result.

14

Figure 13: X-Scan with indicated sample size.

Figure 14: Rocking-Curve with geometry angles.

15

4.2 Measurement

Having completed the adjustments, raw data from the diffusive scan is subtracted from the reflectivity scan to correct for scattering effects which otherwise decrease the signal to noise ratio. This step is depicted in Figure 15.
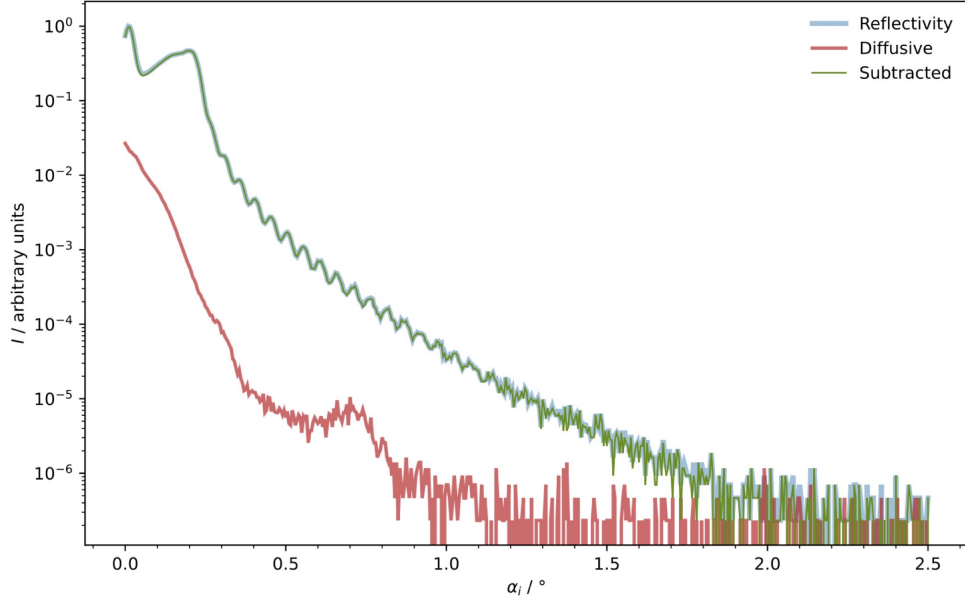
Figure 15: Intensity curves for reflectivity and diffusive background.

Proceeding from this, the calculated intensity is divided by the geometry factor (11) to correct for less than complete beam obstruction. The resulting curve is displayed in Figure 16 and shows a plateau of total reflection below a critical angle

$$\alpha_c = (0.21 \pm 0.01)° \, .$$

The shaded region represents unity reflectivity $R = 1$ and therefore allows one to use the average intensity in this range $I = 1.8 \pm 0.2$ as a normalization factor. Identifying $\alpha_c \cong \sqrt{2\delta}$, the dispersion

$$\delta = (6.4 \pm 0.6) \times 10^{-6}$$

can serve as an initial guess for the corresponding parameters in the recursive Parratt formalism. Additionally, equation (3) can be used to estimate the electron density

$$\rho_e r_e = (1.7 \pm 0.2) \times 10^{11} \, \text{cm}^{-2} \, .$$

By evaluating the Kiessig peaks in Figure 17, one finds the layer thickness via (6).
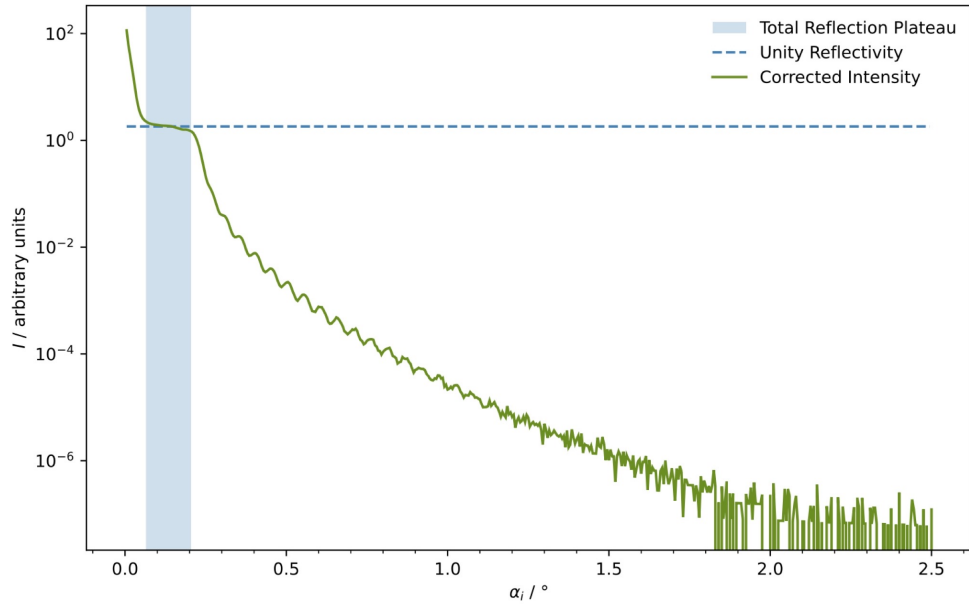
Figure 16: Intensity after geometry factor correction and region of total reflection.
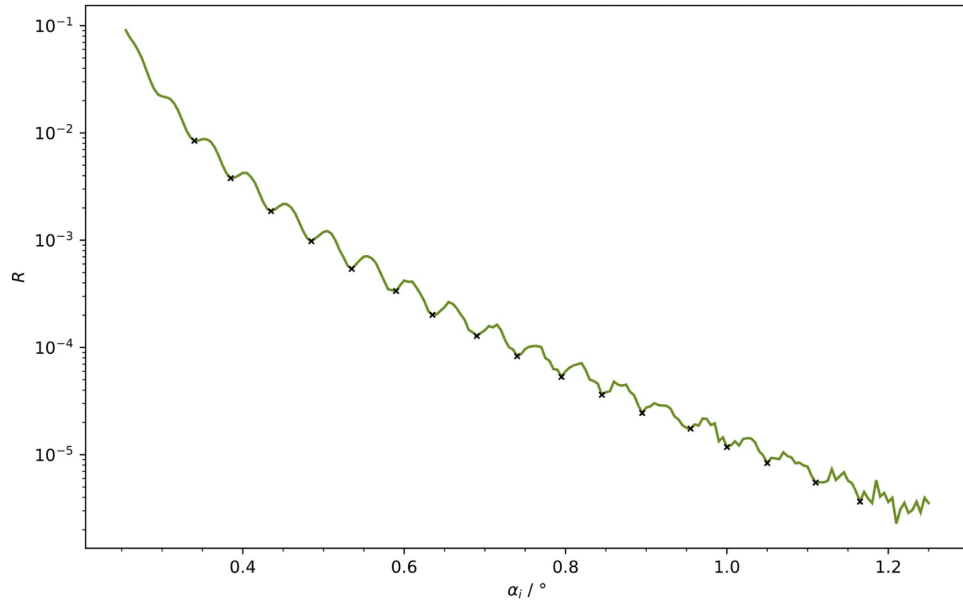
Figure 17: Detailed reflectivity curve with Kiessig oscillation minima.

17

To this end, the average angular distance $\Delta\alpha_i = (0.052 \pm 0.005)°$ between adjacent minima with wavelength $\lambda = 1.5406 \times 10^{-10}\,\mathrm{m}$ for the Cu K_α emission line yields

$$d = (8.6 \pm 0.8) \times 10^{-8}\,\mathrm{m}\,.$$

Finally, Figure 18 includes two fits to the observed reflectivity. First, a Fresnel curve for an ideally smooth Si surface is plotted according to (5) with parameters
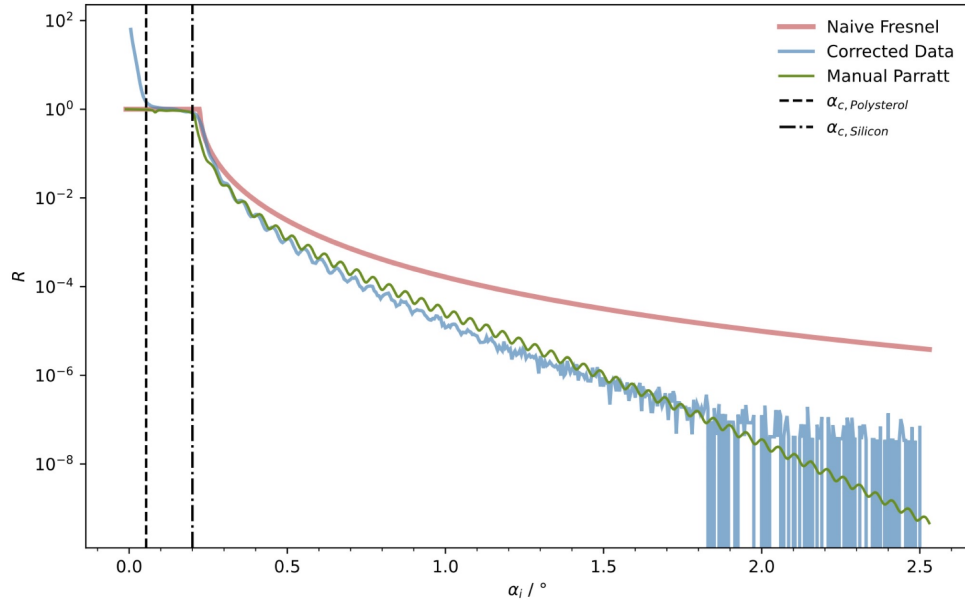
$$\delta = (7.6 \pm 2.3) \times 10^{-6}\,, \qquad\qquad \beta = (0.0 \pm 0.4) \times 10^{-6}\,.$$

Furthermore, a manual optimization of the Parratt algorithm is performed based on the previously obtained input quantities, arriving at

$$\begin{aligned}
\delta_1 &= 7.3 \times 10^{-7}\,, & \delta_2 &= 6.6 \times 10^{-6}\,, \\
\beta_1 &= 4.1 \times 10^{-9}\,, & \beta_2 &= 1.6 \times 10^{-7}\,, \\
\sigma_{01} &= 8.3 \times 10^{-10}\,\mathrm{m}\,, & \sigma_{12} &= 8.1 \times 10^{-10}\,\mathrm{m}\,, \\
d_1 &= 8.6 \times 10^{-8}\,\mathrm{m}\,.
\end{aligned}$$

From these, one finds

$$\begin{aligned}
\alpha_{c,1} &= 0.069°\,, & \alpha_{c,2} &= 0.208°\,, \\
\rho_{e,1} r_e &= 1.93 \times 10^{10}\,\mathrm{cm}^{-2}\,, & \rho_{e,2} r_e &= 1.75 \times 10^{11}\,\mathrm{cm}^{-2}\,.
\end{aligned}$$

Figure 18: Full reflectivity curve with Parratt and Fresnel fits.

5 Discussion

When conducting experiments on physical problems, one often finds differences between measured and calculated values. The same applies here; thus, the following section compares data and calculates deviations. Further, some reasons for inaccuracies are mentioned and briefly discussed.

5.1 Values Measured During the Adjustment Process

During the adjustment process, values such as the sample size were measured. The value derived from the data is calculated to be $D_{\mathrm{exp}} = (21 \pm 3)\,\mathrm{mm}$, while the theoretical value is $D_{\mathrm{theo}} = 20\,\mathrm{mm}$. When comparing these values, a deviation of

$$\frac{\Delta D}{D_{\mathrm{theo}}} = (5.00 \pm 15.00)\,\%$$

can be found. Even though the deviation is not negligible, the experimentally found value encompasses the theoretical value.

These values for D were used to calculate the geometry angle α_g. The deviation between experiment and theory is

$$\frac{\Delta \alpha_g}{\alpha_{g,1}} = (29.63 \pm 37.73)\% \,.$$

Even though the differences between the values of D are not very significant, the resulting geometry angles show considerable deviation. The deviation of the value found using the theoretical value of D, even though it is larger than $1/4$, still encompasses the data from the experiment.

5.2 Comparison of Experimental Results for Silicon and Polystyrene Layers

Literature values for the given materials are given as

$$r_e\rho_{\mathrm{Si,lit}} = 20 \times 10^{10}\ \mathrm{cm}^{-2}\,,$$
$$r_e\rho_{\mathrm{Poly,lit}} = 9.5 \times 10^{10}\ \mathrm{cm}^{-2}\,,$$
$$\delta_{\mathrm{Si,lit}} = 7.6 \times 10^{-6}\,,$$
$$\delta_{\mathrm{Poly,lit}} = 3.5 \times 10^{-6}\,,$$
$$\alpha_{c,\mathrm{Si,lit}} = 0.174°\,,$$
$$\alpha_{c,\mathrm{Poly,lit}} = 0.153°\,.$$

The comparison of experimental values for Polystyrene (Layer 1) and Silicon (Layer 2) with literature values reveals significant deviations. Polystyrene shows a 79.7% deviation in electron density $r_e\rho$, and Silicon shows a 12.5% deviation. The dispersion coefficient

δ for Polystyrene deviates by 79.1%, while Silicon's value has a 13.2% deviation. The critical angle α_c for Polystyrene deviates by 54.9%, and for Silicon, the deviation is 19.5%.

The observed discrepancies are likely caused by a combination of factors, including potential impurities and measurement inaccuracies. In addition to these, the evaluation methods used in the analysis may have introduced inaccuracies.

5.3 Parratt-Algorithm

The evaluation of the Parratt algorithm for X-ray reflectometry presents several challenges and nuances. Utilizing programmatic fitting often proves unsatisfactory for the Parratt algorithm. Instead, manual optimization is time-consuming and inaccurate. A global fit is also difficult to achieve, as it often trades accuracy between critical and higher angles. Additionally, high-angle measurements tend to be very noisy, making it hard to determine what exactly should be fitted.

When considering the parameters, it becomes evident that dispersions control the height of oscillations and the shape of the critical angle cutoff. Extinctions have smaller effects on the curve shape and influence minor features such as a slight peak below the critical angle. The roughness of the outer layer determines the smoothness and prominence of fringes, especially at larger angles. Inner layer roughness affects the height of the curve, particularly at larger angles, while thickness influences the spacing and prominence of the fringes.

These aspects highlight the need for careful analysis and optimization of parameters to achieve meaningful results when applying the Parratt algorithm in X-ray reflectometry. The challenges of manual and global fitting, along with the significance of each parameter, must be considered to obtain precise and reliable outcomes.

References

[1] Jens Als-Nielsen and Des McMorrow. "X-rays and their interaction with matter". In: *Elements of Modern X-ray Physics*. John Wiley & Sons, Ltd, 2011. Chap. 1, pp. 1–28. ISBN: 9781119998365. DOI: `https://doi.org/10.1002/9781119998365.ch1`.

[2] Jens Als-Nielsen and Des McMorrow. "Sources". In: *Elements of Modern X-ray Physics*. John Wiley & Sons, Ltd, 2011. Chap. 2, pp. 29–67. ISBN: 9781119998365. DOI: `https://doi.org/10.1002/9781119998365.ch2`.

[3] Jens Als-Nielsen and Des McMorrow. "Refraction and reflection from interfaces". In: *Elements of Modern X-ray Physics*. John Wiley & Sons, Ltd, 2011. Chap. 3, pp. 69–112. ISBN: 9781119998365. DOI: `https://doi.org/10.1002/9781119998365.ch3`.

[4] L. G. Parratt. "Surface Studies of Solids by Total Reflection of X-Rays". In: *Phys. Rev.* 95 (2 July 1954), pp. 359–369. DOI: `10.1103/PhysRev.95.359`.

[5] Heinz Kiessig. "Interferenz von Röntgenstrahlen an dünnen Schichten". In: *Annalen der Physik* 402.7 (1931), pp. 769–788. DOI: https://doi.org/10.1002/andp.19314020702.

[6] Frank Schreiber and Alexander Gerlach. "X-Ray and Neutron Reflectivity for the Investigation of Thin Films". In: 2004. URL: https://api.semanticscholar.org/CorpusID:4117744.

[7] Metin Tolan. *X-Ray Scattering from Soft-Matter Thin Films*. Springer Berlin, Heidelberg, 1999. ISBN: 978-3-540-49525-3. DOI: https://doi.org/10.1007/BFb0112834.

[8] *V44, X-ray reflectrometry*. TU Dortmund, Department of Physics. 2024.

[9] *Python*. Version 3.11.0. Oct. 24, 2022. URL: https://www.python.org.

[10] Charles R. Harris et al. "Array programming with NumPy". In: *Nature* 585.7825 (Sept. 2020), pp. 357–362. DOI: 10.1038/s41586-020-2649-2. URL: https://doi.org/10.1038/s41586-020-2649-2.

[11] Pauli Virtanen et al. "SciPy 1.0: Fundamental Algorithms for Scientific Computing in Python". Version 1.9.3. In: *Nature Methods* 17 (2020), pp. 261–272. DOI: 10.1038/s41592-019-0686-2.

[12] John D. Hunter. "Matplotlib: A 2D Graphics Environment". Version 1.4.3. In: *Computing in Science & Engineering* 9.3 (2007), pp. 90–95. DOI: 10.1109/MCSE.2007.55. URL: http://matplotlib.org/. Current version 3.6.2, DOI: 10.5281/zenodo.7275322.

[13] Eric O. Lebigot. *Uncertainties: a Python package for calculations with uncertainties*. Version 2.4.6.1. URL: http://pythonhosted.org/uncertainties/.

Appendix